# Formation of talin-vinculin pre-complexes dictates maturation of nascent adhesions by accelerated force transmission and vinculin recruitment

**Sangyoon J. Han[1,2*], Kevin M. Dean[3], Austin J. Whitewood[4], Alexia Bachir[5], Edgar Guttierrez[6], Alex Groisman[6], Alan R. Horwitz[5,7], Benjamin T. Goult[4] and Gaudenz Danuser[1*]**

[1]Lyda Hill Department of Bioinformatics, University of Texas Southwestern Medical Center. Dallas, TX 75390. USA.

[2]Department of Biomedical Engineering, Michigan Technological University. Houghton, MI. 49931. USA.

[3]Department of Cell Biology, University of Texas Southwestern Medical Center. Dallas, TX. 75390. USA.

[4]School of Biosciences, University of Kent, Canterbury, Kent, CT2 7NJ, UK.

[5]Department of Cell Biology, University of Virginia. Charlottesville, VA. 22904. USA.

[6]Department of Physics, University of California San Diego. San Diego, CA. 92093. USA.

[7]current address: Allen Institute for Cell Science. Seattle, WA. 98109. USA.

*Corresponding Author: sjhan@mtu.edu, gaudenz.danuser@utsouthwestern.edu (Lead Contact)

**Abstract**

Talin, vinculin, and paxillin are mechanosensitive proteins that are recruited early to nascent integrin-based adhesions (NAs). Using machine learning, high-resolution traction force microscopy, single-particle-tracking and fluorescence fluctuation time-series analysis, we find that, only in the NAs that eventually mature to focal adhesions, all three molecules are recruited concurrently and in synchrony with force onset. Thereafter, vinculin assembles at ~5 fold higher rates than in non-maturing NAs. We identify a domain in talin, R8, which exposes a vinculin-binding-site (VBS) without requiring tension. Stabilizing this domain via mutation lowers tension-free vinculin binding in conjunction with talin, impairs maturation of NAs, and reduces the rate of additional vinculin recruitment after force onset. Taken together, our data show that talin forms a complex with vinculin, before association with integrins, which is essential for NA maturation by talin's effective unfolding and exposure of additional VBSs that induce fast force growth and further vinculin binding.

## Introduction

Cell-matrix adhesions are multi-molecular complexes that link the extracellular matrix (ECM), typically via integrin transmembrane receptors, to the actin cytoskeleton. Being both a force-transmitter and a force-sensor, cell-matrix adhesions are critical to cell morphogenesis and mechanosensation (Discher et al., 2005; Parsons et al., 2010). Indeed, in response to ECM changes, adhesions undergo constant changes in morphology and motion that involve recruitment and recycling of a large number of adhesion molecules. For example, nascent adhesions (NAs) emerge within the actin-dense cell lamellipodia and then slide in the direction opposite to the protrusion as a result of polymerization-driven flow of the actin network (Parsons et al., 2010). Many of these NAs, which are less than 0.5 μm long, and thus in a light microscope only resolved as diffraction-limited spots, turn over early; but some of them mature into longer focal complexes (FCs, >0.5 μm in length) and focal adhesions (FAs, >2 μm in length) at the lamellipodia-lamella interface (Gardel et al., 2010; Parsons et al., 2010). During this progression, NAs go through multiple decision processes regarding fate and morphology. Compared to the well-studied FAs, for which the interconnection between structure, signaling, and force transmission is largely understood (Balaban et al., 2001; Chrzanowska-Wodnicka and Burridge, 1996; Geiger et al., 2009; Han et al., 2012; Kanchanawong et al., 2010; Plotnikov et al., 2012; Riveline et al., 2001; Stricker et al., 2011; Thievessen et al., 2013), much less is known about the molecular and mechanical factors that determine NA assembly, turnover, and maturation. Until recently, it has also not been technically feasible to measure whether individual NAs bear traction forces. By applying high refractive-index soft substrates that are compatible with total internal reflection microscopy (Gutierrez et al., 2011) and numerical methods for the computational reconstruction of cell-substrate traction at the single micron length-scale, we recently postulated that, like FAs, force transmission is essential for the stabilization and maturation of NAs (Han et al., 2015). However, it remains unknown which factors determine whether a NA begins to bear forces and thus continues to assemble.

One possible factor is the stoichiometry among the earliest molecular components recruited to a NA (Digman et al., 2009; Zaidel-Bar et al., 2004). In particular, the recruitment of talin, vinculin, and paxillin could play a critical role as they all are known to be mechanosensitive (Austen et al., 2015; Carisey et al., 2013; del Rio et al., 2009; Humphrey et al., 2014; Humphries et al., 2007; Kumar et al., 2016; Pasapera et al., 2010; Schiller et al., 2011). Talin is an integrin activator (Moser et al., 2009; Tadokoro et al., 2003) that directly links integrins to the actin cytoskeleton (Calderwood et al., 2013). Under force, the helix bundle domains in talin's rod-like region unfold (del Rio et al., 2009), which both disrupts ligand binding and exposes cryptic binding sites for vinculin and other proteins (del Rio et al., 2009; Goult et al., 2018; Goult et al., 2013; Yan et al., 2015; Yao et al., 2016). Vinculin, when bound to talin's exposed binding sites, can indirectly strengthen the connection between actin and integrins by 1) forming a catch bond with F-actin(Case et al., 2015; Huang et al., 2017), 2) forming multiple linkages from a single talin to multiple F-actin filaments (Atherton et al., 2015; Yan et al., 2015; Yao et al., 2016), and 3) stabilizing talin's unfolded state (Yao et al., 2014). In this scenario, talin must bind to integrins and F-actin first, followed by unfolding and vinculin recruitment under initial tension. Indeed, at the level of FAs, direct evidence for catch-bonds (Bell, 1978; Thomas, 2008; Thomas et al., 2008), and the exposure of hidden binding sites under load (Vogel and Sheetz, 2006; Zhu et al., 2008), have established the idea of force-assisted adhesion growth. Further evidence for this model

indicates that downregulation of actomyosin contractility reduces the recruitment of vinculin (Pasapera et al., 2010) and other adhesion proteins (Kuo et al., 2011), as well as the association between talin and integrins (Bachir et al., 2014).

In contrast to the notion of FA growth and stabilization in a hierarchy talin-first-then-vinculin, fluorescence fluctuation analyses (Bachir et al., 2014) and co-immunoprecipitation experiments (Pasapera et al., 2010) suggest that in NAs talin and vinculin might form a complex before talin associates with integrin. While talin-vinculin pre-association implies vinculin's force-independent binding to talin, it is not clear whether this pre-association is required for NA assembly, and if so, whether the pre-association affects the decision processes for NA maturation. Moreover, paxillin, a scaffolding protein that works in close relationship with focal adhesion kinase (FAK) (Mitra and Schlaepfer, 2006; Parsons, 2003; Pasapera et al., 2010; Schlaepfer and Mitra, 2004), is thought to be recruited and stabilized by force at an early phase of NA assembly (Choi et al., 2008; Deakin and Turner, 2008; Plotnikov et al., 2012; Schiller et al., 2011); the relationship to vinculin recruitment remains to be established (Laukaitis et al., 2001; Webb et al., 2004; Wiseman et al., 2004).

Here, we investigate the role of molecular recruitment and mechanical forces in determining the fate of NAs. We combined high-resolution traction force microscopy for measuring the force levels in every NA with those of the sensitive and particle tracking of the recruitment of fluorescently labeled molecules to NAs to acquire time courses of force transmission and molecular composition at individual adhesions. A comprehensive inventory of these traces revealed broad heterogeneity in NA behaviors. We applied machine learning approaches to divide NAs into subgroups with distinct characteristics, determining that five subgroups are necessary to account for the different kinematic, kinetic and mechanical properties of NAs. Focusing on the NA subgroup maturing into stable FAs, we found that the formation of a talin-vinculin pre-complex was mediated by talin's R8 domain. These pre-complexes enforce the link between talin and actin, likely to allow the unfolding of talin and exposure of additional vinculin binding sites, which ultimately supports the transition of spontaneous molecular assemblies of in nascent adhesions into stable macromolecular focal adhesions.

## Results

### *Nine adhesion classes can be distinguished based on different kinetic, kinematic and mechanical behaviors*

To investigate time courses of traction and adhesion protein recruitment, we performed two-channel time-lapse, total internal reflection fluorescence (TIRF) imaging of Chinese Hamster Ovary epithelial cells (ChoK1, Fig 1a-f). For each experiment, images of beads, with the reference bead image of undeformed gel configuration, were processed for traction reconstruction using high-resolution TFM software, as described before (Han et al., 2015). As expected for a contractile cell, all traction vectors pointed from the cell periphery to the center, regardless of which adhesion protein was co-imaged (Fig 1a-c). Fluorescently tagged adhesion proteins (Fig 1d-f) were detected and tracked, and their intensity time courses extracted from the trajectories (Fig. 1g). Accounting for the heterogeneity of adhesions, we collected 22 features from each trajectory (Fig. 1h, Table S1). Based on these features, we classified the adhesion trajectories into nine groups (see Table S2 for a summary of each group). To this end, we implemented a supervised machine learning pipeline, where a human operator labeled, with the support of a dedicated graphical user

interface, ~120 adhesion tracks (at least 10 tracks per group) out of ~10,000 tracks per movie. These data were then used to train a support vector machine (SVM) classifier (validation accuracy: 70 – 80 %, Fig. S1a). All features were inspected for redundancy and similarity (Fig. S1b-c), and each group was distinct in terms of its Euclidian distance to the closest group in the feature space (Fig. S1d). SVM-based classification of all trajectories that were excluded from the training data assigned each adhesion to one of nine different classes, G1, G2, …, G9 (Fig. 1i). Five of the nine classes (G1-G5) identified NAs, three (G6-G8) identified FAs, and one group (G9) contained insignificant, noise-like trajectories (Movie S1). The five NA classes significantly differed in terms of features such as “edge protrusion speed” (Fig. 1j), “adhesion movement speed” (Fig. 1k), “average fluorescence intensity” (Fig. 1l), and “lifetime” (Fig. 1m). For example, NAs classified into G3 form at the tip of the protruding edge and move forward with the protrusion. Of all NA classes, their fluorescence amplitude is lowest (Fig 1j-m). NAs classified into G2 form at the protruding edge but slide rearward relative to the substrate and mature to form larger FCs or FAs. They have the highest intensity and longest lifetime (Fig 1m-n). NAs classified into G1 also form at the protruding edge, but they stay relatively stationary (Fig. 1k) with a weak fluorescence intensity and a short lifetime (Fig. 1m-n).

Next, we tested the hypothesis that these spatially and kinetically distinguished groups generate distinct traction. Indeed, we found that the subgroup of maturing NAs, G2, shows highest traction magnitude shortly after initial assembly. This is consistent with previous findings about tension-mediated maturation of FAs (Choi et al., 2008; Schiller et al., 2011; Schiller et al., 2013). Interestingly, NAs in G3 exhibited an insignificant amount of traction without ever significantly increasing (Fig. S2), suggesting this population consists of assemblies of adhesion proteins that do not engage with the substrate. NAs in G1 had higher traction than those in G3, implicating that short-living, non-maturing NAs can transmit significant amount of traction, consistent with our previous finding (Han et al., 2015). These trends in traction as well as trends in feature variables after classification were consistent regardless of which adhesion protein was used for tracking (talin, vinculin or paxillin; Fig. S3). Altogether, these results confirm the reliability of the classifier and suggest that kinetically unique NAs also show mechanical differences.

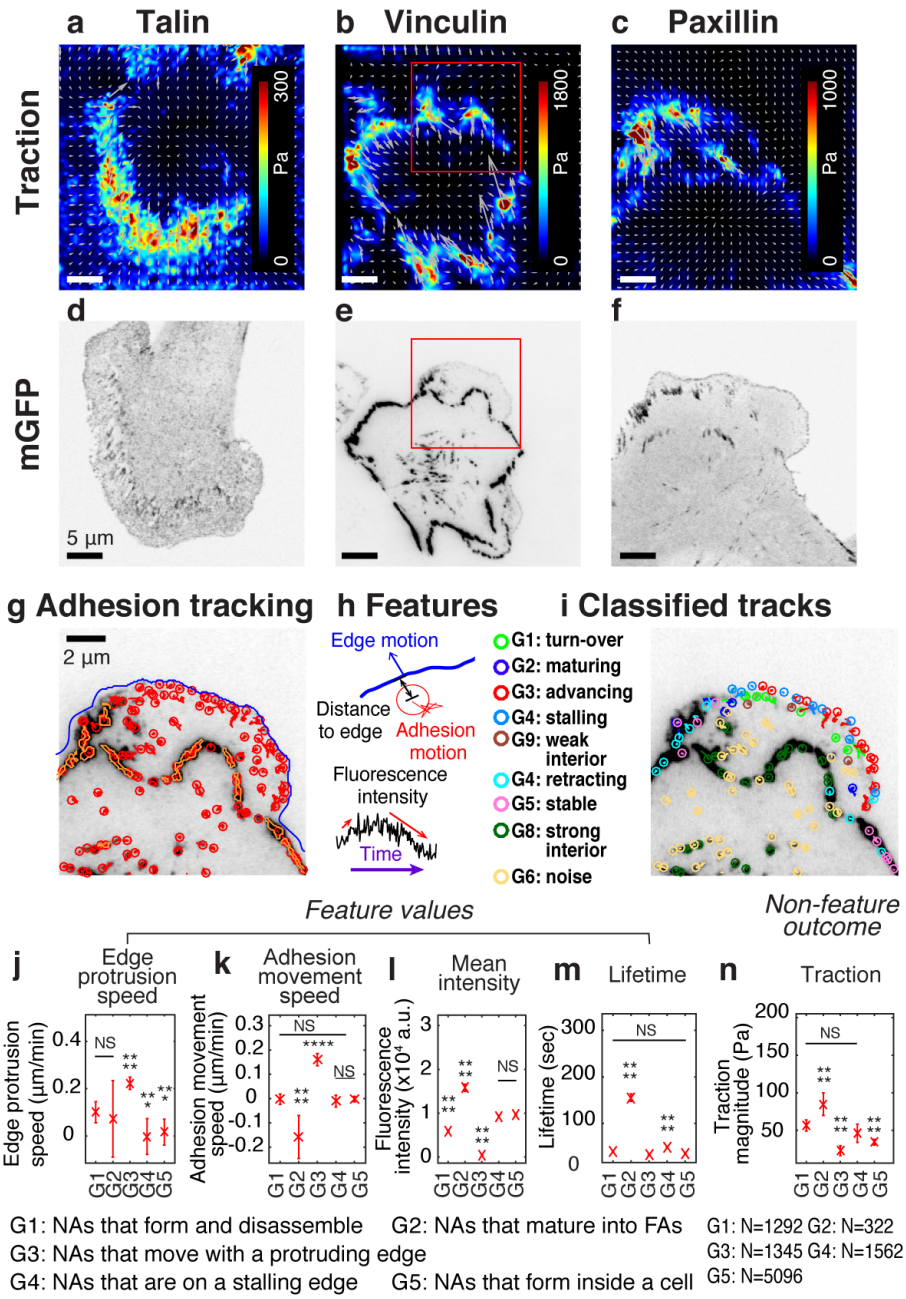


*Figure 1* Experimental/computational framework to analyze heterogeneous adhesion dynamics in ChoK1 cells. (a – c) high-resolution traction maps co-imaged with mGFP-tagged adhesion protein, talin (d), vinculin (e), and paxillin (f). 5 kPa silicone gel coated with high density beads was used as a TFM substrate. (g) Trajectories of individual nascent and focal adhesions overlaid on a region of interest cropped from (e). Tracking is based on all detected point sources, (red circles). Big segmented focal contacts/adhesions (orange, closed freeform overlays) were used as additional information for feature selection. (h) Some of the key features used for supervised classification, tabulated in Table 1. (i) Classification of adhesion trajectories into nine different groups, overlaid on the adhesion image. Five different NA groups, three FA groups and one noise group were distinguished using the error-correcting output codes classifier, multiclass model for support vector machines (L. Allwein et al., 2001). (j-m) Comparison of feature values among the five NA groups, G1, G2, G3, G4 and G5: edge protrusion speed (j), adhesion movement speed, positive when sliding toward protruding edge (k), mean intensity (l), and lifetime (m), extracted from six vinculin-tagged cells. All features show a significant shift in value for at least one subgroup. (n) Average traction magnitude, read from traction map, at individual NA trajectories per each group. The number of samples per each group is shown in the lower right corner of the figure.

*Talin, vinculin and paxillin are recruited sequentially in non-maturing NAs, but concurrently in maturing NAs with traction development*

To evaluate the relationship between molecular recruitment and traction force in NAs, we performed high-resolution traction force microscopy on cells labeled with talin, vinculin, or paxillin, and processed these data using the aforementioned classifier (Movies S1-S9). We focused our analysis on the differences between NAs in G1 (non-maturing) and G2 (maturing, Fig. 2). For all proteins evaluated, fluorescence intensity traces in G1 had a lifetime of ~6-7 min, with clear rising and decaying phases (Fig. 2a-f, top). The associated traction traces exhibited intermittent rises and falls with an overall magnitude much smaller than the traction traces in G2 (Fig. 2a-f, bottom). As expected, NAs in G2 showed a steady increase in both fluorescence intensity and traction traces with a lifetime greater than 15 minutes (Fig. 2g-l). The fluorescence intensity and traction of individual G1 and G2 NAs reflected this stereotypical behavior, and so did the average behavior, i.e. a slight increase and fall for G1 and more steady increase for G2 (Fig. S4a-i). A further analysis with cohort plots, where traces of similar lifetime are grouped and separately displayed, revealed that average traces of many cohorts follow the stereotypical behavior (Fig. S4j-o).

Next, we developed an event-based time-series analysis method that identifies the first time point of significant fluorescence and force increase, respectively, and then measures the time shift between the two (Fig. 2m). The blue and red arrows in Fig. 2d-f, j-l show, in two example traces, the time points identified statistically as the first intensity increase and the first traction increase, respectively. Using this approach, we first determined the fraction of NAs per group with a significant traction increase at any point throughout their lifetime (Fig. S5). Interestingly, both G1 and G2 NAs showed such a force increase, i.e. they were engaging at one point with the substrate. NAs in groups G3-5 exhibited lower fractions of force increases, suggesting that a very large number of adhesion protein aggregates, detectable through either talin, vinculin, or paxillin recruitment, never engage with the substrate.

Focusing then on the NAs in group G1 and G2, we analyzed the protein recruitment sequences using the initial force increase as a fiduciary. In non-maturing NAs (G1), talin and vinculin were recruited ~18 sec and ~8 sec before the onset of force transmission, respectively, whereas paxillin recruitment coincided with the onset of force transmission (Fig. 2n). In maturing NAs (G2), talin, vinculin and paxillin were recruited concurrently with the onset of force transmission (Fig. 2o). We also noted that the temporal distributions of protein recruitments were significantly wider in G1 adhesions than in G2 adhesions, and that of the three measured proteins, talin had by far the widest temporal recruitment window. These findings suggested that in G2 adhesions talin might form a pre-complex with vinculin prior to its association with integrin, which leads to force transmission and progression into maturation. In contrast, although G1 adhesions eventually also support some lower level of force transmission (Fig. 1n), talin and vinculin assemble sequentially in a long waiting period under force-free conditions.

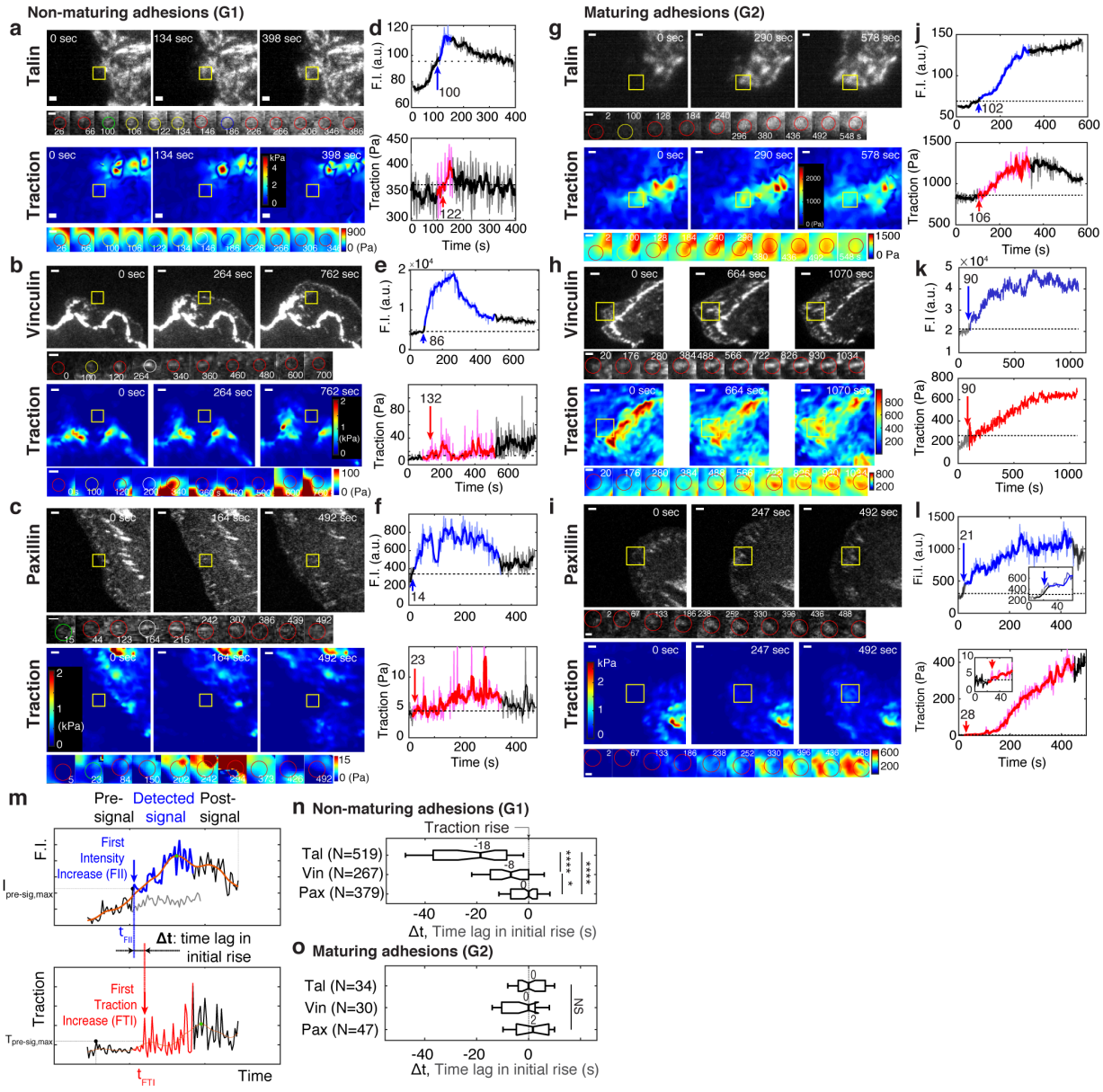


Figure 2 *Talin and vinculin in non-maturing NAs are recruited in a sequential manner before traction development whereas they are recruited at the same time, along with paxillin, concurrent with the initial traction rise in maturing NAs.* (a-l) Representative traces of talin, vinculin, and paxillin for non-maturing (a,b,c), or maturing (g,h,i) NAs. Yellow boxes show position of the example adhesions in time lapse image sequences of mGFP-tagged talin (a,g, top), vinculin (b,h, top), and paxillin (c,i, top) and associated traction maps (a-c, g-i, bottom). Scale bar: 1 um. (d-l) Traces of fluorescence intensity (top) and traction (bottom). Periods of significant fluorescence intensity of the tagged proteins are indicated in blue for fluorescence intensity and red for traction. An inset in (l) indicates that also in this trace the traction is gradually increasing. Blue and red arrows mark the time points of the first intensity increase (FII) and the first traction increase (FTI), respectively, which are defined in (m). (m-o) Analysis of time-shifts between protein recruitment and FTI. (m) Traces of fluorescence intensity (top) and traction (bottom). Illustrated is the detection of the first significant value in both series. Distinct distributions of time lags between FII and FTI in non-maturing (n) and maturing (o) NAs. Sample numbers, extracted from 6 cells for talin, 5 cells for vinculin and 4 cells for paxillin, are shown in each y-axis label. *: $p<1x10^{-2}$, ****: $p<1x10^{-30}$ by Mann-Whitney U test

*In maturing NAs, vinculin assembles faster than in non-maturing NAs, but talin and paxillin show no difference*

The rod domain of talin contains 13 helical bundles, 9 of which include cryptic vinculin binding sites (VBSs) that are exposed after mechanical unfolding under tension(del Rio et al., 2009; Geiger et al., 2009; Goult et al., 2013). Thus, we hypothesized that the simultaneous talin-vinculin recruitment in maturing NAs could result in accelerated further vinculin binding compared to non-maturing NAs. To test this, we quantified the assembly rate of each protein by obtaining the slope of the fluorescence intensity over the first 10 sec after initial appearance (Fig. 3a). Interestingly, only vinculin showed a significant difference in the assembly rate between non-maturing vs. maturing vinculin complexes, while talin and paxillin showed no such differences (Fig. 3a). Thus, with a talin-vinculin pre-complex involved in G2 NA formation, talin could be more amenable to unfolding additional VBS-containing domains, which in turn would reinforce further vinculin recruitment and adhesion maturation. We also quantified the traction force growth in those NAs with an expectation that there would be an immediate rise in force with faster vinculin binding. However, the traction force growth rate for the first 10 seconds showed no significant difference between non-maturing vs. maturing NAs (Fig. 3b). Nevertheless, a difference was observed when the force growth rate was quantified over a longer period, i.e., two minutes (Fig. 3c), consistent with our previous finding (Han et al., 2015). These findings imply that increased vinculin recruitment in maturing NAs – because of the effective tension development across the talin/vinculin mediated linkage between integrin and F-actin – supports the rise of traction force by connecting the protein complex to more F-actin, with some time delay.

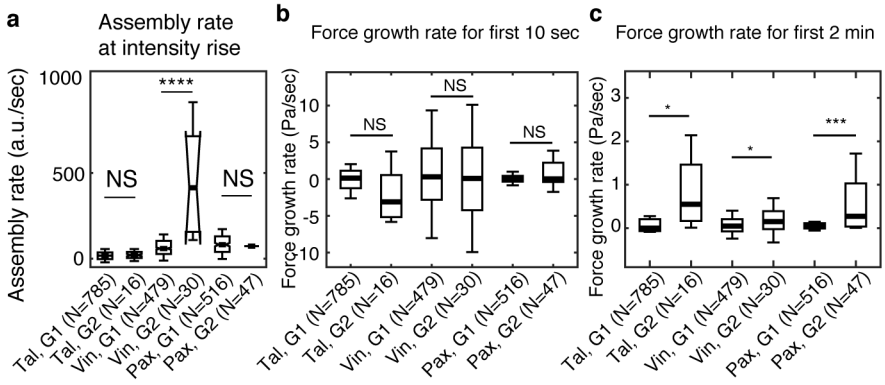


*Figure 3 Vinculin, but not talin and paxillin, is recruited significantly faster in maturing NAs than in non-maturing NAs.* (a) Assembly rate of talin, vinculin and paxillin, to G1 (non-maturing) or to G2 (maturing) NAs, quantified as the slope of fluorescence intensity over the initial 10 seconds after detection. (b) Traction force growth rate of the NAs in (a) for the initial 10 seconds after detection. (c) Force growth rate quantified over the first two minutes after detection. *: $p<1x10^{-2}$, ***: $p<1x10^{-10}$, ****: $p<1x10^{-30}$ by Mann-Whitney U test

*Vinculin can bind to talin without force through a 'threonine belt' in talin R8 domain*

Previous work established that under tension the talin R3 domain unfolds first, as it contains a destabilized hydrophobic core due to the presence of a 'threonine belt' of four threonine residues. By mutating the threonine residues to isoleucines and valines (the so called "IVVI mutant") it was possible to stabilize the core and prevent talin from unfolding, which significantly reduces the exposure of the two VBS (Elosegui-Artola et al., 2016; Goult et al., 2013; Yao et al., 2014). Moreover, we had shown that the VBS in R8 was able to bind vinculin readily in the absence of force (Gingras et al., 2010). Like R3, R8 also contains a threonine belt, consisting of T1502, T1542 and T1562 (Fig. 4a)(Yan et al., 2015). Thus, we hypothesized that a similar strategy, using a

T1502V, T1542V, T1562V "R8vvv mutant", could stabilize the R8 domain and reduce the VBS activity. To test this hypothesis, we made a "R7R8vvv" construct and compared its unfolding characteristics to wild-type R7R8 fragment (R7R8wt) using circular dichroism (CD; Fig. 4b). We included the R7 domain to make the fragment more stable and better behaved than R8 alone and to maintain R8 in its native conformation, In the R7R8wt the two domains unfolded cooperatively with a single unfolding step at a melting temperature ($T_m$) of 55°C. In contrast, stabilization of the R8 domain in the R7R8vvv mutant resulted in the domains unfolding independently, with R7 unfolding at a similar temperature to the wt ($T_m$ 56°C), but the temperature of R8 domain increased from 56°C to 82°C. Strikingly, the two unfolding steps indicate that in the R7R8vvv mutant the R7 and R8 behave independently with regard to thermal stability. Together, these results show that the R7R8vvv mutant stabilizes R8.

To test whether stabilization of R8 would affect its interaction with vinculin, we used analytical gel filtration to look at complex formation. Preincubation of both R7R8wt and R7R8vvv with vinculin Vd1 showed both constructs were able to form complexes with vinculin, however the R7R8vvv:Vd1 complex peak was substantially smaller than the wildtype:Vd1 peak, confirming that the R7R8vvv was less able to bind to Vd1 (Fig. 4c). This finding suggested that accessibility of the VBS was reduced with stabilization of the threonine belt by valine replacement. To further quantitate the interaction, we used microscale thermophoresis (MST), titrating the talin proteins against RED-tris-NTA labeled Vd1. R7R8wt bound with a relatively high affinity of 2.07μM whereas, under the same conditions, we were not able to detect any binding to R7R8vvv (Fig. 4d). The R8 domain is also an LD-motif binding site, i.e. it binds to multiple LD proteins including RIAM and DLC1(Goult et al., 2018; Goult et al., 2013; Zacharchenko et al., 2016). Using a fluorescence polarization assay described previously(Whitewood et al., 2018), we measured the binding affinities of R8 ligands RIAM TBS1 and DLC1 peptides with R7R8wt and R7R8vvv (Fig. S6). Both peptides bound to the R7R8vvv with comparable affinities to the wildtype R7R8, confirming the R7R8vvv was still able to bind LD-motif proteins. Altogether, these biochemical characterizations of the R7R8vvv mutant suggested that the threonine belt in talin R8 is responsible for vinculin binding without force. The mutant also provided a tool for us to probe the functional implications of talin-vinculin pre-complex formation on NA assembly and maturation *in vivo* without interfering with binding of other binding partners.

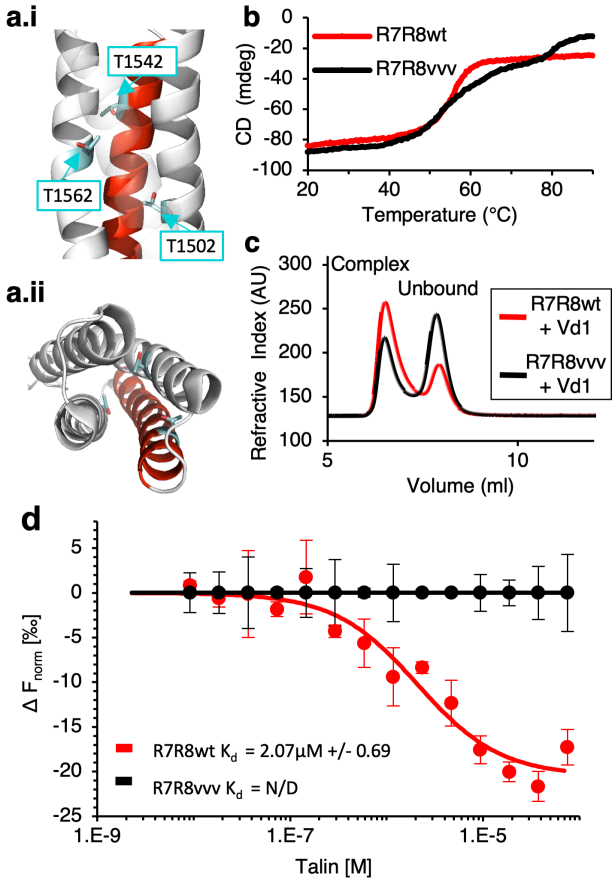


Figure 4 *Stabilizing the "threonine belt" in the R8 domain of talin inhibits talin-vinculin interactions under tension-free conditions*. (a) Cartoon representation of talin R7R8 (pdb id 2X0C) showing the 'threonine belt', comprised of residues T1502, T1542, and T1562, labeled and shown as sticks (cyan), the VBS helix is colored red. (a.i) side on view (N.B. helix 31 transparent), (a.ii) top down view. (b) Denaturation profiles for wildtype R7R8wt (red) and R7R8vvv (black) measured by monitoring the change in circular dichroism at 208 nm with increasing temperature. R7R8wt has a melting temperature of 55°C, whereas R7R8vvv unfolds in two steps, one (R7) with a melting temperature of 56°C and R8 unfolding at 82°C. (c) Chromatograms showing binding of talin R7R8 to the vinculin head (Vd1). R7R8wt (red) and R7R8vvv (black) binding to Vd1. Complex peaks and unbound peaks are indicated. (d) MST analysis of R7R8wt (red) and R7R8vvv (black) interaction with Vd1. Experiments were done in triplicate and analysed using the $K_d$ fit model on NanoTemper analysis software. Dissociation constants +/- SE (µM) for the interactions are indicated in the legend. ND not determined.

### *Cells with R8vvv mutant talin show less maturing NAs and sparser and smaller FAs*

To investigate whether the ability of talin to form a pre-complex with vinculin promotes adhesion maturation, we introduced the R8vvv mutation into full-length talin1, in addition to tagging the protein with the mNeonGreen fluorescent protein. We named this construct "talin1 R8vvv-mNG". To express this talin mutant, we prepared talin1 KD ChoK1 cells using shRNA and rescued with sh-resistant forms of talin1 R8vvv-mNG, or WT talin1-mNG as a control. The expression of talin1 R8vvv-mNG was slightly less than that of WT ChoK1 cells but more than talin1 KD Chok1 cells (Fig. S7). We imaged the mNeonGreen signal of talin1 R8vvv mutant or WT talin1 of each cell on 5 kPa gel along with high-resolution traction force analysis. Cells with talin1 R8vvv-mNG contained many more NAs (Fig. 5a,b,f,g,k) and less and smaller FCs and FAs (Fig. 5a,b,f,g,l,m) than control cells with WT talin1-mNG. Cells expressing the talin1 R8vvv-mNG also showed less traction compared to WT the talin1-mNG rescue condition (Fig. 5c,h,n). With less traction and

more NAs, edge protrusion and retraction of cells with talin1 R8vvv-mNG were faster than cells with WT talin1-mNG (Fig. 5d,i). Moreover, a lower fraction of NAs and FCs in R8vvv mutant cells grew in size to FAs than NAs in cells with WT talin1 rescue (Fig. 5e,j,o,p). Together, these results demonstrate that talin R8vvv mutation restricts NAs from maturing into focal adhesions.

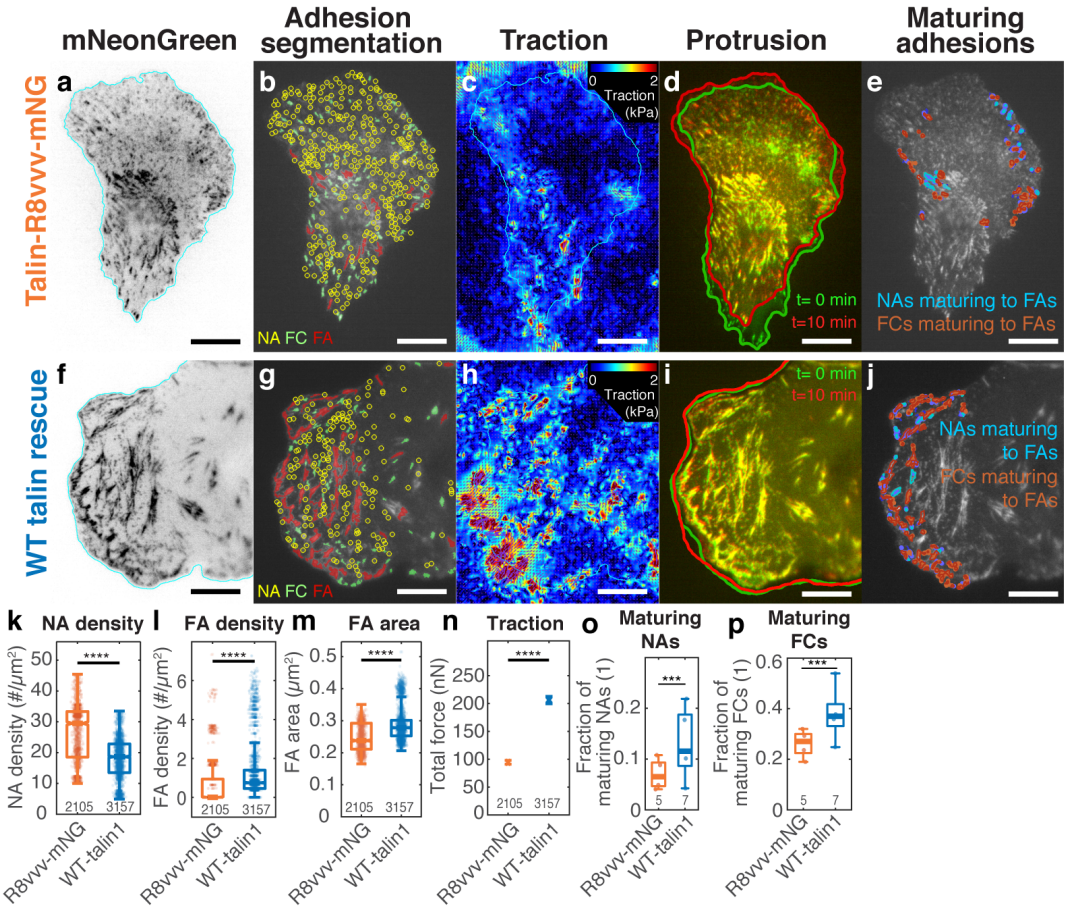


Figure 5 *Expression of the talin1 R8vvv mutant results in formation of denser NAs, but lesser and smaller FAs, lower traction, more active protrusion and less maturing adhesions compared to expression of the talin wildtype.* (a-j) Adhesion, traction and protrusion phenotype of a representative ChoK1 cell on 5 kPa gel substrates expressing talin R7R8vvv mutant (a-e) vs a representative ChoK1 cell expressing WT talin (f-j). (a,f) inverted talin-mNeonGreen images. (b,g) detection of NAs, FCs and FAs. (c,h) traction maps. (d,i) snapshots of computer vision-extracted cell boundaries at 0 and 10 min of a movie. (e,j) overlay of NAs and FCs that mature to FAs. (k-m) Box plots of NA density (k), FA density (l), and FA area (m). (n) Total traction integrated over cell area. Numbers of adhesions collected from M=5 and M=7 independently imaged cells for talin1 R8vvv-mNG and WT talin1-mNG rescue, respectively, are indicated under each box plot. (o, p) Box plots of the fraction of NAs maturing to FAs relative to all NAs (o) and of the fraction of FCs maturing to FAs (relative to all FCs) (p). Here, N=5 and 7 are the number of independently imaged cells. Scale bar: 10 µm. ****: $p<1x10^{-30}$ by Mann-Whitney U test

*R8vvv mutation does not affect talin recruitment but impedes traction growth rate*

To investigate whether talin pre-complex formation with vinculin affects talin recruitment itself, we compared the time of talin recruitment in talin1 R8vvv mutant cells vs. WT talin1 rescue cells for non-maturing (G1) and maturing (G2) NAs. Consistent with the data in Fig. 3, in both cell types G1 adhesions showed talin recruitment, on average, ~14 sec prior to the initial rise in traction (Fig. 6a,c,e,g,i), while G2 adhesions showed a near coincidental talin recruitment (Fig. 6b,d,f,h,i). This indicates that the ability of talin to bind vinculin does not affect talin recruitment. For both WT and R7R8vvv mutant talin, the assembly rates were statistically indistinguishable between non-

maturing and maturing NAs (Fig. 6j). The rate of traction development in NAs, however, was significantly affected in talin1 R8vvv-mNG mutant cells. Overall, the traction increase was reduced in mutant cells, both for G1 and G2 (Fig. 6k). Moreover, while in WT talin1 rescue cells G2 NAs showed faster traction growth than G1 NAs, consistent with the data in Fig. 3c, in talin1 R8vvv-mNG mutant cells G2 adhesions exhibited an even slower force growth than G1 NAs. These results suggest that the talin-vinculin pre-complex is essential for the development of force across NAs, which is required for further adhesion maturation.

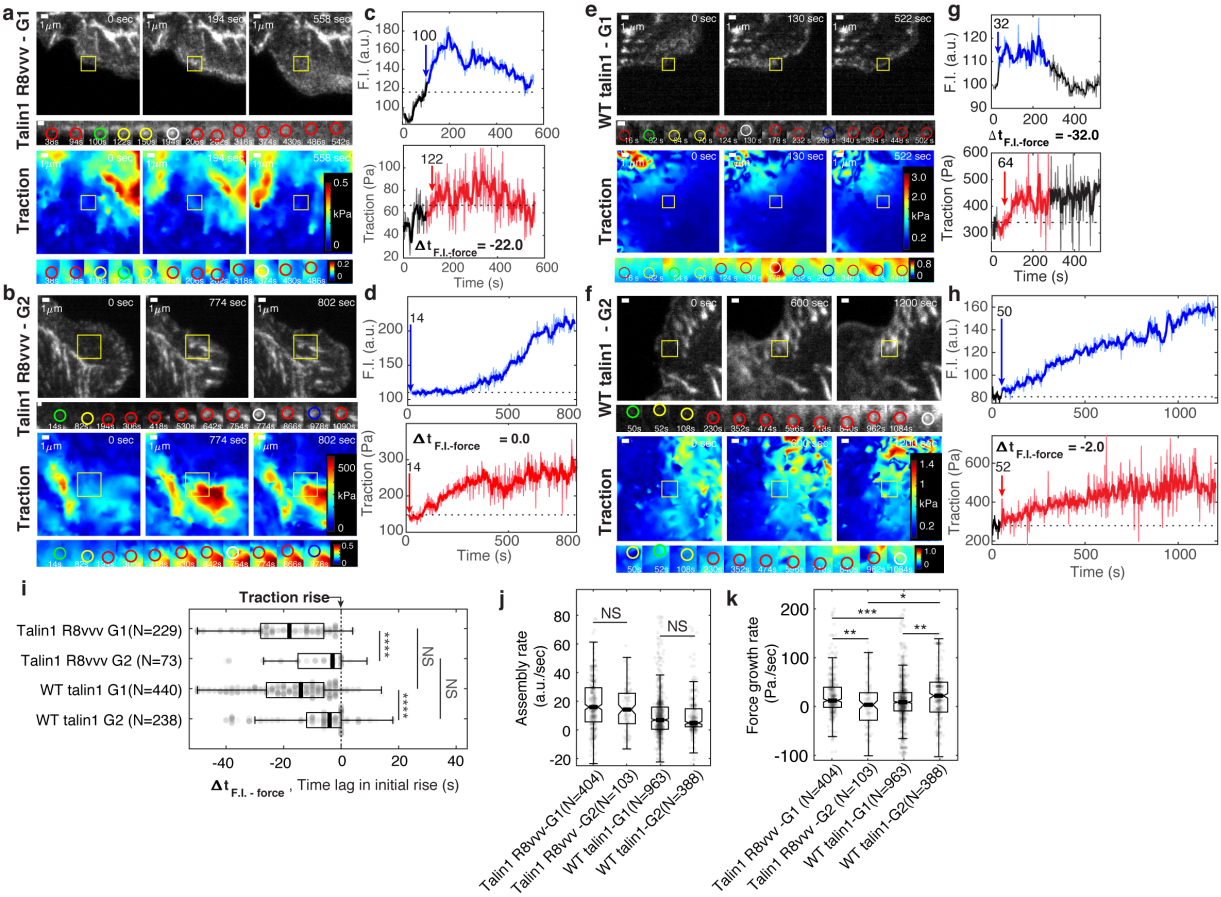


*Figure 6 Expression of talin1 R8vvv-mNG mutant does not change the recruitment timing of talin to NAs, but reduces the force growth rate in NAs.* (a-h) Representative talin and traction force images of talin1 R8vvv-mNG expressing cells (a-d) and WT talin-mNG rescue cells (e-h) within non-maturing (a,c,e,g) and maturing (b,d,f,h) NAs. (a,b,e,f) talin-mNeonGreen images (top) and traction images (bottom) of three different time points, i.e. at initial nucleation, at maximum fluorescence intensity, and at the end of the NA portion of the track. Yellow boxes on both images and traction maps indicate the position of a representative NA, for which a time lapse sequence is assembled in the bottom row. Scale bar: 1 µm. (c-d, g-h) Traces of talin-mNeonGreen fluorescence intensity (top) and traction (bottom). Phases of the traces with significant fluorescence above background are indicated in blue and red, respectively. Blue and red arrows mark the time points of the first intensity increase and the first traction increase, respectively (i-k) Distributions of time lags of fluorescence intensity onset relative to traction onset (i), talin assembly rates (j), and traction growth rates (k) of non-maturing (G1) and maturing (G2) NAs in talin1 R8vvv-mNG mutant and WT talin1-mNG rescue cells. *: $p<1x10^{-2}$, **: $p<1x10^{-3}$, ***: $p<1x10^{-10}$, ****: $p<1x10^{-30}$ by Mann-Whitney U test

## *Differential vinculin recruitment between non-maturing vs. maturing NAs vanishes with talin1 R8vvv mutation*

Vinculin recruitment to the NA is critical for both force growth and adhesion maturation (Fig. 3) (Thievessen et al., 2013). To examine whether the assembly rate of vinculin is affected by talin's ability to form a pre-complex with vinculin, we performed two-channel imaging of vinculin-SnapTag-TMR-Star and WT talin1 or talin1 R8vvv mutated talin-mNeonGreen (see Methods). As for prior analyses, we captured and analyzed time-series of each pair of talin-vinculin signals in non-maturing vs. maturing NAs (Fig. 7a-h) and quantified the vinculin assembly rate within 30 seconds after first detection (Fig. 7i). In talin1 R8vvv-mNG mutant cells, vinculin assembly rates were statistically indistinguishable between non-maturing (G1) and maturing (G2) NAs, whereas in WT talin1-rescue cells vinculin rates were significantly higher in G2, consistent with the data acquired in control cells (Fig. 3a). This result suggests that early vinculin binding to talin R8 domain indeed contributes to faster recruitment of additional vinculins. The insignificant difference in vinculin recruitment in R7R8vvv mutant cells for G1 vs. G2 NAs might be related to the reverted traction growth rates between the two NA groups observed in these mutant cells (Fig. 6k). It is also worth noting that the vinculin signal in G2 NAs of cells with WT talin-rescue tended to keep increasing while talin intensity was relatively flat (t=200~600 sec in Fig. 7h,d), suggesting that the number of exposed talin VBSs is increasing over time under tension. The same trend was observed in talin1 R8vvv mutant cells (Fig. 7b,f), but the vinculin recruitment rate was again much less than those found in WT talin1-rescue. Altogether, this data strongly suggest that vinculin recruitment is significantly reduced when no vinculin-talin pre-complex can form.

*Simultaneous talin-vinculin imaging confirms vinculin's recruitment after talin for non-maturing NAs and concurrent recruitment for maturing NAs*

To confirm the recruitment order of talin and vinculin with respect to traction force development (Fig. 2), we quantified the time difference between the first significant increase in talin fluorescence intensity and the first significant increase in vinculin fluorescence intensity (blue and magenta arrows in Fig. 7a-h, j). At non-maturing NAs, both in talin1 R8vvv mutant and WT talin1-rescue cells, vinculin was delayed to talin on average by ~10 seconds (Fig. 7j), consistent with the delay we inferred indirectly based on alignment of the fluorescent intensity increases with the first significant traction force increase (Fig. 2n). At maturing NAs, vinculin and talin recruitment coincided (Fig. 7j), also consistent with the indirect inference presented in Fig. 2n. This shows directly that the formation of a talin-vinculin pre-complex indeed enhances the probability of NA maturation. In more detail, vinculin recruitment in maturing NAs of talin1 R8vvv mutant cells was ~4 seconds after talin recruitment, whereas vinculin recruitment in WT talin rescue condition preceded the talin recruitment by ~2 seconds (Fig. 7j). We interpret this difference as the result of the mutation in talin's R8 domain, which reduces the ability of vinculin to bind talin prior to mechanical unfolding. Moreover, even though some maturing NAs eventually grow also in talin1 R8vvv mutant cells, the absence of efficient vinculin binding to the VBS in R8 propagates into an overall less efficient vinculin recruitment. In agreement with this interpretation, we found that the lifetimes of maturing G2 NAs in the mutant cells were much shorter than those in cells with WT-talin1 rescue (Fig. 7k). Altogether, our data establishes that talin's pre-association with vinculin via the talin R8 domain is critical for accelerated vinculin binding, which in turn contributes to the development of the level of force transmission required for NA maturation.

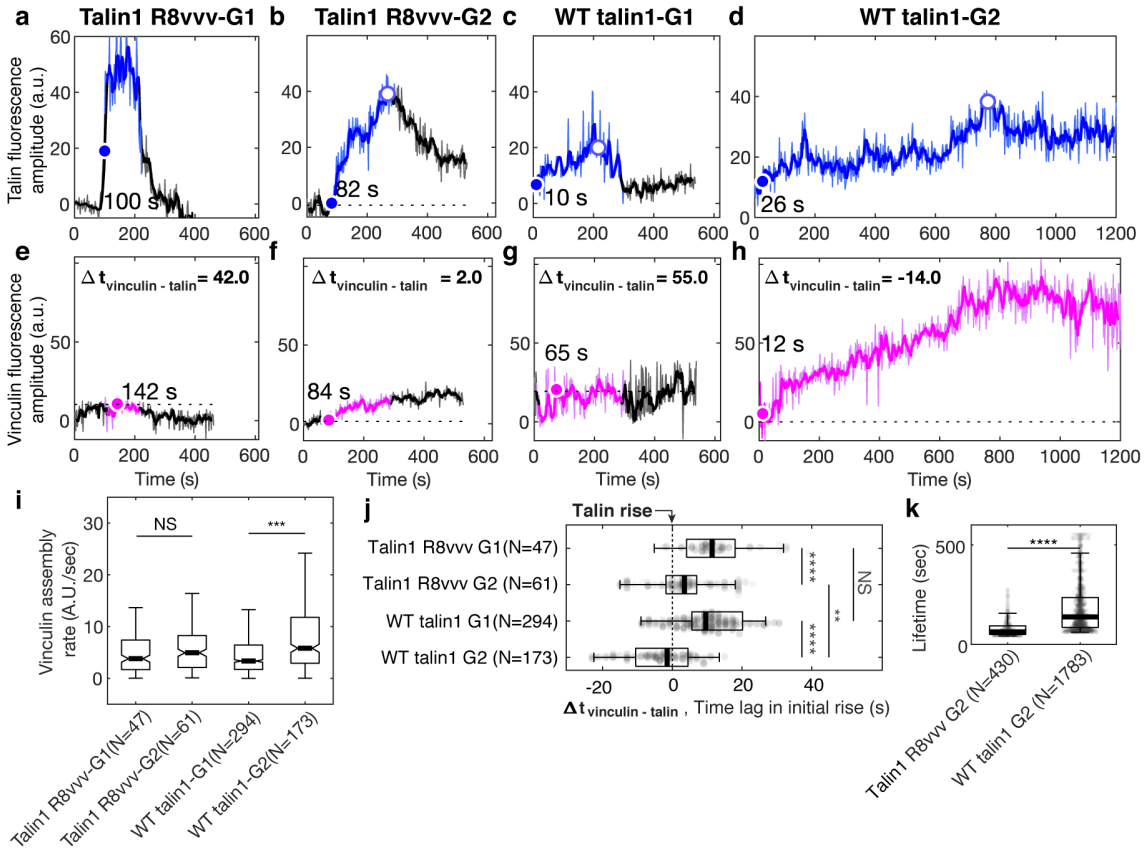


*Figure 7 Vinculin recruitment is reduced in talin1 R8vvv mutant cells.* (a-h) Representative traces of talin-mNeonGreen (a-d) and vinculin-SnapTag-TMR-Star (e-h) fluorescence intensity at G1 non-maturing (a,c,e,g) and G2 maturing (b,d,f,h) NAs in cells expressing the talin1 R8vvv mutant (a-b, e-f) and WT talin (c-d, g-h) constructs. Phase of the traces with significant intensity above background are shown in color (blue for talin, magenta for vinculin). Blue and magenta arrows indicate the time of talin and vinculin recruitment onset, respectively. (i) Vinculin assembly rates at non-maturing and maturing NAs in R7R8vvv mutant and WT talin rescue cells, quantified by the slope of vinculin-SnapTag-TMR-Star fluorescence intensity over the initial 30 seconds after the first detection in the talin-mNeonGreen channel. (j) Time delays of vinculin recruitment onset relative to talin recruitment onset of non-maturing vs. maturing NAs in talin1 R8vvv-mNG mutant and WT talin1 mNG cells. Vinculin recruitment onsets in non-maturing NAs are positive, i.e. vinculin recruitment starts after talin. In contrast, vinculin recruitment onsets in maturing NAs are nearly coincidental with talin. See the text for further description. (k) Lifetimes of maturing NAs classified in talin1 R8vvv mutant and WT talin1 mNG rescue cells. ****: $p<1x10^{-30}$ by Mann-Whitney U test. The numbers of adhesions (N), extracted from 7 cells each for cells with talin1 R8vvv-mNG and WT talin1-mNG, are shown per each condition name at each panel.

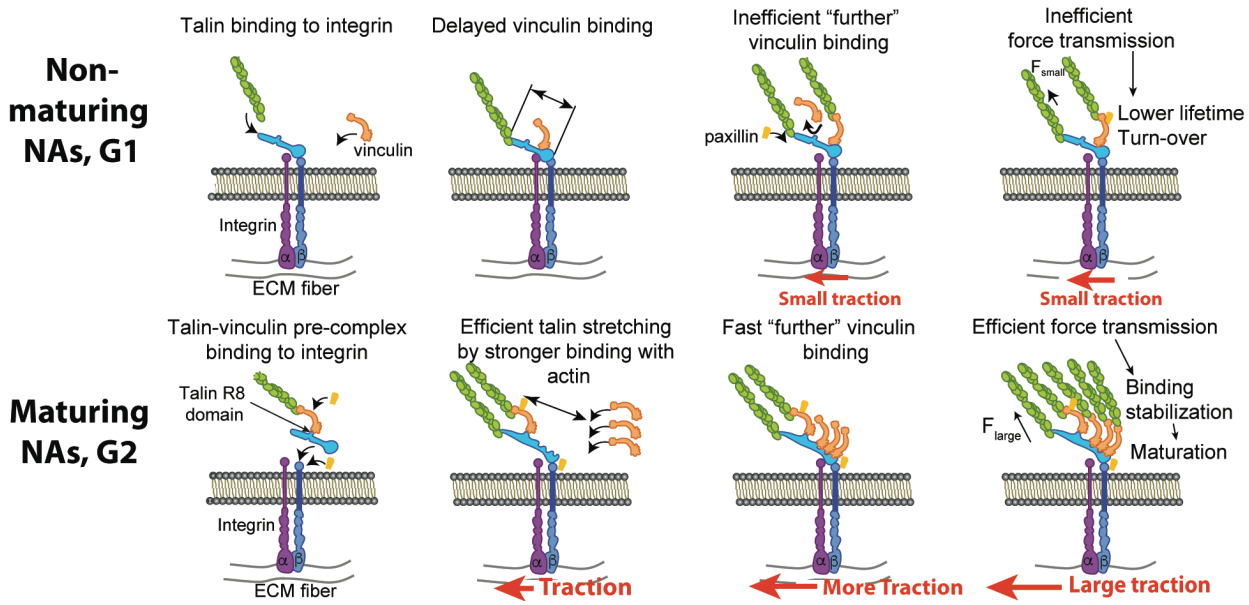


Figure 8 *A suggested mechanism of differential recruitment of talin and vinculin determining maturation of nascent adhesions.* (Top) For non-maturing NAs, talin binds to integrin before vinculin recruitment. Talin stretching is limited to a shorter level, which limits the exposure of vinculin-binding-sites. Inefficient vinculin binding, in turn, limits the number of F-actin that can connect to the adhesion complex, allowing for only a low amount of tension across the complex. Insufficient loading level reduces the lifetime of catch-bond like associations between molecules, resulting in turnover of the NA complex. (Bottom) For maturing NAs, talin and vinculin form a pre-complex before association with integrin. Upon pre-complex recruitment to the NA traction force builds immediately. Talin is stretched in a faster manner by pre-associated vinculin and talin's own binding to F-actin accommodate faster, efficient recruitment of additional vinculin. High loading levels across the complex stabilizes molecular bonds, which facilitates the maturation of the NA.

## Discussion

Our experiments show that the maturation of NAs depends on the formation and recruitment of a talin-vinculin pre-complex. Previous models have inferred that tension across talin, which can establish direct bridges between integrins and actin filaments, is sufficient to unfold the molecule and expose several vinculin binding sites. These binding sites were thought to promote the recruitment of vinculin to further strengthen the link between the integrin-talin complex and actin (Goult et al., 2018; Sun et al., 2016). However, these models were derived primarily from observations in focal adhesions, i.e. at a late stage of the maturation process (Atherton et al., 2015; Thievessen et al., 2013). Here, we exploit our ability to concurrently measure traction and molecular associations at the scale of individual NAs using total internal reflection microscopy on high-refractive index soft substrates (Gutierrez et al., 2011; Han et al., 2015). Our data suggests that the tension borne by an individual talin bridge between integrin and actin filaments is insufficient to fully unfold the talin rod domain and expose the number of VBSs necessary for talin to form a stable link to F-actin. This further lowers the lifetimes of catch-bond-like molecular associations (Hakonardottir et al., 2015; Huang et al., 2017; Sun et al., 2016) between talin and vinculin, vinculin and actin, and talin and actin, resulting in turnover of the NAs (Fig. 8, top). In contrast, pre-assembled talin-vinculin complexes immediately establish a strong link between integrin and F-actin, as indicated by the concurrent recruitment of talin and vinculin and traction force onset. The fast loading rate promotes a fast and efficient unfolding of the talin rod domain, which exposes several additional VBSs for further recruitment of vinculin and strengthening of the talin/F-actin interaction. This results in robust increase of traction force transmission and

stabilization of catch-bond-like molecular associations that contribute to the maturation of the NA (Fig. 8, bottom).

Our data show that the formation of a talin-vinculin pre-complex is promoted by talin's R8 domain, which contains a VBS that is exposed for vinculin recruitment without tension-mediated unfolding of talin. We generated a talin mutant with a more stable R8 domain that prevents spontaneous association with vinculin. Cells expressing this mutant have a large fraction of NAs that cannot mature into FAs and transmit only low-level forces. This identification is different from previous findings, including ours, where talin's R3 domain has been described as the weakest domain that can unfold under tension (Atherton et al., 2015; Yao et al., 2016). Thus, we speculate that in maturing NAs, vinculin's R8 binding leads to unfolding of R3, followed by exposure of additional VBSs in R1-R2. Our data suggest that the fraction of maturing NAs must be initiated with this R8-mediated talin-vinculin pre-complex. Intriguingly, pre-complex formation prior to incorporation into adhesion requires spontaneous encounters of mobile talin and vinculin at the plasma membrane or even in the cytosol. These are likely rare events, which may explain the surprising finding that the number of maturing (G2) NAs (3.5 ± 1.6 %, Mean ± Standard Error of the Mean, N=20 movies) is so low compared to G1 NAs (28.8 ± 3.5 %, Mean ± S.E.M., N=20 movies) among all NAs.

Our data also indicates that paxillin is recruited concurrently with the onset of traction force regardless of the fate of a NA (Fig. 2). This means that, especially in non-maturing NAs, paxillin is recruited after vinculin. Tension dependency of paxillin recruitment is well-established (Schiller et al., 2011). Our data suggests that tension-dependent recruitment of paxillin is through vinculin, which is consistent with a previous finding that paxillin recruitment can be induced by vinculin (Humphries et al., 2007) as it binds to the tail-domain of vinculin (Turner et al., 1990). Alternatively, paxillin has been reported to be recruited after focal adhesion kinase (FAK) in endothelial cells (Hu et al., 2014). Given evidence that talin can also be recruited by FAK (Lawson et al., 2012), paxillin's recruitment after talin and vinculin might be coincident with vinculin-paxillin binding mediated by FAK. In line with our measurements, a FRET-based tension sensor study has shown that of the three molecules paxillin, talin and vinculin, paxillin levels correlate strongest with traction force levels (Morimatsu et al., 2015). Altogether, our findings agree with previous evidence that paxillin levels are an accurate reporter of traction levels but is not an early protein to indicate the nucleation of NAs.

In the case of non-maturing NAs, talin and vinculin were recruited significantly before our measurements could detect a significant traction onset. This finding implies that there are sub-populations of talin and vinculin that carry only little force. Additionally, talin is present for a longer time than vinculin before traction onset in non-maturing adhesions. While this is conceptually consistent with a previous finding that vinculin binding to talin requires talin's actin binding for tension development (Austen et al., 2015), the time lag between talin and vinculin recruitment suggests that talin's sole engagement with F-actin without vinculin potentially impedes talin's own role as an integrin activator (Shattil et al., 2010) and promoter of integrin clustering (Saltel et al., 2009). Additionally, before vinculin binding, talin may be bound to the Rap1-interacting adaptor molecule (RIAM) (Lee et al., 2009), which is replaced by vinculin once talin's R2R3 domain unfolds (Goult et al., 2013).

How the talin-vinculin pre-complex can promote faster tension development and talin unfolding in maturing adhesions remains to be determined. Potential mechanisms imply: 1) that

the complex is also pre-bound to F-actin through the vinculin tail as vinculin bound to talin is almost certainly in an open conformation (Golji and Mofrad, 2013; Humphries et al., 2007); and 2) that the talin-vinculin interactions via talin's R8-domain do not interfere with talin's direct binding to F-actin, thus accelerating talin's actin-binding rate. Additionally, in maturing adhesions paxillin is recruited concurrently with the talin-vinculin pre-complexes. A paxillin-binding-site in vinculin's tail domain has not been co-localized with paxillin when studied with a vinculin-tail fragment (Humphries et al., 2007). Our data suggests a possibility that a full-length vinculin in a living cell might be immediately associated with paxillin upon its pre-complex formation with talin (Carisey and Ballestrem, 2011).

In summary, our work establishes an unexpected role for a talin-vinculin pre-complex as a mechanical prerequisite to the further recruitment of vinculin to talin, which is the foundation of adhesion maturation. While the possibility of talin-vinculin pre-complexes has been discussed in previous studies (Bachir et al., 2014; Pasapera et al., 2010), their function has remained obscure. Here, we now show that this complex formation is an essential step in adhesion assembly. Where this complex forms and whether the formation is regulated by cellular signals are two of the critical questions to be addressed in future studies.

## Materials and Methods

### Cell Culture

ChoK1 cells were cultured in Dulbecco's Modified Eagle Medium (DMEM) with 4.5 g/L D-Glucose, L-Glutamine, and Sodium Pyruvate (Gibco, 11995-065) supplemented with 10% Fetal Bovine Serum (Equitech-Bio, Inc, SFBU30), 1% Anti-Anti (Gibco, 15240112), and 1% Non-Essential Amino Acids (Gibco, 11140076). For transfection, cells were plated in a 6-well plate at ~30% confluency and transfected the next day with 350 ng of fluorescent protein-, or SNAP-tagged adhesion marker, 1 µg of pBluescript (Stratagene) as non-specific DNA, 10 µL of Lipofectamine LTX (Gibco, 15338030), and 2 mL of reduced serum Opti-MEM (Gibco, 31985088) according to the manufacturer's directions. Four hours after adding the DNA-lipid mixture to the cells, the media was replaced with full DMEM media. 24 hours later, cells were trypsinized, and enriched with flow cytometry for low-level GFP-positive cells. Of this pool, 50,000 cells were seeded on fibronectin-coated (see below) traction-force microscopy substrates in pH 7.4 HyQ-CCM1 media (GE Lifesciences, SH30058.03), supplemented with 1.2 g/L of sodium bicarbonate and 25 mM HEPES. mGFP-talin1 (provided by N. Bate and D. Critchley), paxillin-eGFP (provided by I. Schneider), and mGFP-vinculin (provided by M. Humphries) were used for adhesion-TFM two-channel experiments.

For knock-down experiments, a previously validated shRNA hairpin against talin (GGAAAGCTTTGGACTACTA) was stably introduced into ChoK1 cells with a pLVX-shRNA1 lentiviral system and selected for with 5 µg/mL of puromycin. Western blot analysis indicated decreased levels of talin expression (Figure S7). For rescue experiments, talin was subcloned into the pCDNA3.1(+) mammalian expression vector (ThermoFisher Scientific, V79020), and silent mutations were introduced into the corresponding shRNA target sequence for both the WT talin1-mNG and the talin1 R8vvv-mNG constructs. The R8 mutations (T1502V, T1542V, and T1562V, according to mouse numbering), alter the stability of the talin R8 domain. For vinculin imaging, mNeonGreen (Allele Biotechnology) was replaced with SNAP-Tag using seamless cloning, and labeled with SNAP-Cell TMR-Star (New England Biolabs, S9105S) or SNAP-Cell

647-SiR (New England Biolabs, S9102S) according to manufacturer's recommendations. All protein-coding regions of expression constructs were verified with traditional primer walking and Sanger sequencing.

***Expression of recombinant polypeptides.***

For in vitro analyses, murine vinculin Vd1 (residues 1–258), murine talin R7R8wt (residues 1357-1653) and R7R8vvv (residues 1357-1653; T1502V, T1542V and T1562V) were cloned into a pET151 vector (Invitrogen) and expressed in E.coli BL21(DE3) cells cultured in LB. Standard nickel-affinity chromatography was used to purify the His-tagged recombinant proteins as described previously(Whitewood et al., 2018). The proteins were further purified using anion exchange chromatography following cleavage of the 6xHis-tag with TEV protease. Protein concentrations were determined using their respective extinction coefficients at 280 nm.

***Circular Dichroism (CD)***

Spectroscopy was performed using a JASCO J-715 spectropolarimeter equipped with a PTC-423S temperature control unit. Denaturation profiles were measured from 20-80°C at 0.2°C intervals by monitoring the unfolding of α-helices at 208 nm. 0.1 mg/mL of protein was dissolved in phosphate buffered saline (PBS). Measurements were made in a quartz cell of 0.1 cm path length.

***Fluorescence polarization assays***

To determine if other binding partners of talin R8 domain except for vinculin can still bind to R7R8vvv fragment, the relative binding affinities were measured using an in vitro fluorescence polarization assay. The R8 interacting, LD-motif containing peptides from DLC1 and RIAM, i.e., DLC1_465-489-C (IFPELDDILYHVKGMQRIVNQWSEK-C) and RIAM_6-30-C (DIDQMFSTL LGEMDLLTQSLGVDT-C), were coupled to a thiol-reactive fluorescein dye via the terminal cysteine. Peptides with a C-terminal cysteine were synthesized by GLBiochem (China). Stock solutions (i.e., peptide + fluorescein) were made in phosphate-buffered saline (PBS; 137 mM NaCl, 27 mM KCl, 100 mM Na2HPO4, 18 mM KH2PO4, pH 7.4), 1 mM TCEP and 0.05% Triton X-100. Excess dye was removed using a PD-10 desalting column (GE Healthcare, Chicago, IL, USA). Titrations were performed in PBS using a constant 1 μM concentration of fluorescein-coupled peptide with increasing concentration of R7R8 fragment (either wild type or vvv mutant); final volume 100 μM in a black 96-well plate. Fluorescence polarization (FP) measurements, in which the binding between the two polypeptides results in an increase in the fluorescence polarization signal, were recorded on a BMGLabTech CLARIOstar plate reader at room temperature and analyzed using GraphPad Prism. $K_d$ values were calculated with nonlinear curve fitting using a one-site total binding model.

***Microscale Thermophoresis (MST) assay***

Recombinantly expressed vinculin head domain (Vd1) was coupled to an equimolar amount of NT-647 dye (RED-tris-NTA NanoTemper) via its N-terminal 6xHis-Tag in a one-step coupling reaction(Tschammer et al., 2016). Titrations were performed in phosphate buffered saline (PBS; 137 mM NaCl, 27 mM KCl, 100 mM $Na_2HPO_4$, 18 mM $KH_2PO_4$) using a constant 50 nM concentration of RED-tris-NTA coupled Vd1, with increasing concentration of recombinantly

expressed talin R7R8wt and R7R8vvv; final volume 20 µL. Prepared samples were filled into Monolith NT.115 Capillaries (NanoTemper). Measurements were recorded on a Monolith NT.115 at 25°C, excited under red light, medium MST power and 40% excitation power. The data was analyzed using MO. Affinity Analysis software (v2.3) and fitted using the Kd fit model.

***Analytical gel filtration***

Gel filtration was performed using a Superdex-75 size exclusion chromatography column (GE Healthcare) at a flow rate of 0.7 mL/min at room temperature in 50 mM Tris pH 7.5, 150 mM NaCl, 2 mM DTT. A sample of 100 µL consisting of 100 µM of each protein was incubated at a 1:1 ratio at 25°C for 10 minutes. The elution was monitored by a Malvern Viscotek SEC-MALS-9 (Malvern Panalytical, Malvern, UK).

***Western blot***

Cells were transfected under identical conditions as they were for imaging experiments but with a 10 cm dish and sorted with a flow cytometer (FACS Aria II SORP) for low expression. Cells were lysed by adding 2x laemmli + 10% b-ME, vortexing, and heating at 95°C for 10 minutes. Protein concentration was measured, and the same amount was loaded for each lane. The gel was semi-dry transferred with a turbo blot, and then incubated overnight in 5% milk in tris-buffered saline with 0.1% Tween 20 (TBST) at 4 degrees. Protein was visualized with an anti-talin antibody at 1:1000 and the loading control was visualized with anti-b-actin at 1:5000, each in 0.5% milk/TBST overnight at 4°C. Gels were then rinsed with TBST, and probed with IgG:horseradish peroxidase in 0.5% milk/TBST at 4°C for 1 hour and then at room temperature for another 30 minutes. Gels were rinsed three times for 20 minutes in TBST and then detected with enhanced chemiluminescence.

**TFM Substrate Preparation**

All silicone substrates had a diameter of 35 mm, a stiffness of 5 kPa, were embedded with 580/605 or 640/647 ($\lambda_{EX}/\lambda_{EM}$) 40 nm-diameter beads, and were compatible with total internal reflection fluorescence illumination. Substrates were coated with fibronectin (Sigma Aldridge, F1141) the same day as imaging experiments were conducted by mixing 20 µL of a 10 mg/mL 1-ethyl-3-(3-dimethylaminopropyl) carbodiimide hydrochloride (EDC) solution, 30 µL of a 5 mg/mL fibronectin solution, and 2 mL of $Ca^{2+}$ and $Mg^{2+}$ containing Dulbecco's Phosphate Buffered Saline (DPBS, Gibco, 14040117) for 30 minutes at room temperature. Thereafter, the substrate was rinsed 2 times with DPBS, and incubated with 2 mL of 0.1% (w/v) bovine serum albumin in DPBS for another 30 minutes at room temperature, and rinsed several times with PBS prior to seeding with 50,000 transiently transfected cells.

**TIRF Imaging for TFM and adhesion proteins**

Cells were imaged with a DeltaVision OMX SR (General Electric) equipped with ring-TIRF, which mitigates laser coherence effects and provides a more homogeneous illumination field. This microscope is equipped with a 60x, NA=1.49, objective, and 3 sCMOS cameras, configured at a 95 MHz readout speed to further decrease readout noise. The acquired images were in 1024x1024 pixel format with an effective pixel size of 80 nm. Imaging was performed at 37°C, 5% carbon dioxide, and 70% humidity. Laser-based identification of the bottom of the substrate was

performed prior to image acquisition, with a maximum number of iterations set to 10. Laser powers were decreased as much as possible, and the integration time set at 200 milliseconds, to avoid phototoxicity. At the back pupil of the illumination objective, the laser power for both 488 and 568 nm lasers was ~22 mW. Imaging was performed at a frequency of 1 Hz for 5-10 minutes, and deviations between the alignment for each camera were corrected in a post-processing step that provides sub-pixel accuracy. After imaging, cells were removed from the substrate with a 30% bleach solution, and the beads on the relaxed gel substrate were imaged for each cell position. Rapid imaging was necessary to mitigate swelling effects in the silicone substrate and to resolve traction forces in nascent adhesions.

**TFM Force Reconstruction**

Bead images of the deformed gel – acquired when a cell was on the substrate – and a 'reference bead image' of the relaxed gel acquired after cell removal - were processed for traction reconstruction as described previously(Han et al., 2015). Briefly, the bead images of the deformed gel were compared with the reference image using particle image velocimetry. A template size of 17 to 21 pixels, and a maximum displacement of 10 to 80 pixels, depending on the bead density and overall deformation, were used for cross-correlation-based tracking of the individual beads. The displacement field, after outlier removal, was used for traction field estimation over an area of interest. The area of interest on the reference bead image was meshed with square grids of the same width, which depends on the average area per bead. The forward map, which defines the expected deformation of the gel at all bead locations given a unit force at a particular mesh of the force grid, was created by solving Boussinesq Eq. under the assumption of infinite gel depth. This forward map was then used to solve the inverse problem, i.e. given the measured field of bead displacements, the underlying traction field is determined. The solution to this inverse problem is ill-conditioned in that small perturbations in the measured displacement field can yield strong variation in the reconstructed traction field. To circumvent this problem, the traction field was estimated subject to L1-norm regularization. As discussed in detail in (Han et al., 2015), L1-norm regularization preserved the sparsity and magnitude of the estimated traction field. Also as discussed and validated in (Han et al., 2015), the application of L1-norm regularization over the L2-norm regularization most traction force microscopy studies employ is essential to resolve force variation at the length scale of the distances between individual nascent adhesions. The level of regularization is determined by a control parameter. We chose the parameter based on L-curve analysis, which guaranteed a fully automated and unbiased estimate of the traction field (Han et al., 2015). Strain energy, which represents the mechanical work a cell has put into the gel, was quantified as 1/2 × displacement × traction, integrated over a segmented cell area. The unit of this integral is femto-Joule.

**Adhesion segmentation, detection and tracking**

Focal adhesions (FAs) and diffraction-limited nascent adhesions (NAs) were detected and segmented as previously described(Han et al., 2015). Briefly, FAs from images of either labelled paxillin, talin, or vinculin were segmented with a threshold determined by a combination of Otsu's and Rosin's algorithms after image pre-processing with noise removal and background subtraction. Segmented areas larger than 0.2 $\mu m^2$ were considered for focal contacts (FCs) or FAs, based on the criteria described by Gardel et al.(Gardel et al., 2010). Individual

segmentations were assessed for the area and the length, which is estimated by the length of major axis in an ellipse that fit in each FA segmentation. FA density was calculated as the number of all segmentations divided by the cell area. Nascent adhesions were detected using the point source detection described in (Aguet et al., 2013). Briefly, fluorescence images were filtered using the Laplacian of Gaussian filter and then local maxima were detected. Each local maximum was then fitted with an isotropic Gaussian function (standard deviation: 2.1 pixels, i.e. ~180 nm) and outliers were removed using a goodness of fit test ($p$ = 0.05). NA density was defined as the number of NAs divided by the entire cell area.

**Adhesion classification**

From the adhesion tracks, features 1-9 in Table 1 were captured from the individual fluorescence intensity traces, and features 10-21 in Table 1 from the corresponding spatial properties, some in reference to the position and movement of the proximal cell edge and to the overlap with segmentations of focal adhesions and focal complexes. The classification was accomplished using a cubic support vector machine (SVM). The classifier was evolved in a human-in-the-loop fashion, i.e. the user iteratively adjusted machine-generated classifications. The initial training data was labeled with qualitative criteria described in Table 2. To facilitate the labeling process, an automatic, filtering-based, labeling was also employed (see Table 3).

Both manual labeling and automatic labeling have advantages and drawbacks in terms of classification accuracy: while the manual labeling is less consistent due to subjectivity and human error, the automatic labeling has deficiencies in terms of incompleteness of the filtering criteria in capturing all essential properties of different adhesion classes. To overcome these drawbacks, both methods were employed in a way that the automatic labeling was performed first, and then manual labeling was added for insufficiently-labeled classes. During the manual labeling, adhesion classifications were immediately updated and presented to the user to allow class reassignments of selected adhesions. The labeling process was regarded to be completed once at least 10 adhesions were labeled for each class. To remove classification bias due to potential imbalance in the number of labels across the classes, the minority classes were oversampled, and the majority classes were undersampled, based on the mean number of labels (Krawczyk, 2016). After training a classifier on one movie, for a new movie, another iteration of automatic-and-manual labeling was executed to update the classifier, which was applied to predict the classes of adhesions in the movie. Separate classifiers were built for talin-, vinculin-, and paxillin-tagged adhesions.

**Acknowledgement**

We would like to thank Joseph Chi and Dana Reed for preparing DNA constructs and assisting western blot. We also acknowledge Assaf Zaritsky for providing helpful comments about machine learning. This work was funded by the following grants: NIH F32GM117793 (K.M.D.), NIH P01GM098412 (A.G., A.R.H., and G.D.), NIH R01GM067230 (G.D.), Biotechnology and Biological Sciences Research Council grant BB/N007336/1 (B.T.G.) and a Human Frontier Science Program grant RGP00001/2016 (B.T.G.).

**Author contribution**

S.J.H., A.R.H and G.D. conceived the project. K.M.D performed imaging experiments with talin constructs and its variations (e.g. R8vvv mutant). K.M.D. created ChoK1 cells with talin1 shRNA and talin1 R8vvv expression. A.B. performed imaging experiments for WT GFP-tagged vinculin and paxillin. S.J.H designed the experiments and performed TFM reconstruction, nascent adhesion analysis and machine learning from the images. S.J.H. and G.D. wrote the manuscript and S.J.H. made the figures. B.T.G. provided suggestions for talin structure and mutation. A.J.W. and B.T.G. performed biochemical experiments and analyses. Silicone substrates were provided by A.G. and E.G. All authors reviewed and provided feedback on the manuscript.

**Competing Interests**

The authors declare no competing interests.

## References

Aguet, F., Antonescu, C.N., Mettlen, M., Schmid, S.L., and Danuser, G. (2013). Advances in analysis of low signal-to-noise images link dynamin and AP2 to the functions of an endocytic checkpoint. Dev Cell *26*, 279-291.

Atherton, P., Stutchbury, B., Wang, D.Y., Jethwa, D., Tsang, R., Meiler-Rodriguez, E., Wang, P., Bate, N., Zent, R., Barsukov, I.L.*, et al.* (2015). Vinculin controls talin engagement with the actomyosin machinery. Nature communications *6*, 10038.

Austen, K., Ringer, P., Mehlich, A., Chrostek-Grashoff, A., Kluger, C., Klingner, C., Sabass, B., Zent, R., Rief, M., and Grashoff, C. (2015). Extracellular rigidity sensing by talin isoform-specific mechanical linkages. Nat Cell Biol *17*, 1597-1606.

Bachir, A.I., Zareno, J., Moissoglu, K., Plow, E.F., Gratton, E., and Horwitz, A.R. (2014). Integrin-associated complexes form hierarchically with variable stoichiometry in nascent adhesions. Curr Biol *24*, 1845-1853.

Balaban, N.Q., Schwarz, U.S., Riveline, D., Goichberg, P., Tzur, G., Sabanay, I., Mahalu, D., Safran, S., Bershadsky, A., Addadi, L.*, et al.* (2001). Force and focal adhesion assembly: a close relationship studied using elastic micropatterned substrates. Nat Cell Biol *3*, 466-472.

Bell, G.I. (1978). Models for the specific adhesion of cells to cells. Science *200*, 618-627.

Calderwood, D.A., Campbell, I.D., and Critchley, D.R. (2013). Talins and kindlins: partners in integrin-mediated adhesion. Nat Rev Mol Cell Biol *14*, 503-517.

Carisey, A., and Ballestrem, C. (2011). Vinculin, an adapter protein in control of cell adhesion signalling. Eur J Cell Biol *90*, 157-163.

Carisey, A., Tsang, R., Greiner, A.M., Nijenhuis, N., Heath, N., Nazgiewicz, A., Kemkemer, R., Derby, B., Spatz, J., and Ballestrem, C. (2013). Vinculin regulates the recruitment and release of core focal adhesion proteins in a force-dependent manner. Curr Biol *23*, 271-281.

Case, L.B., Baird, M.A., Shtengel, G., Campbell, S.L., Hess, H.F., Davidson, M.W., and Waterman, C.M. (2015). Molecular mechanism of vinculin activation and nanoscale spatial organization in focal adhesions. Nat Cell Biol *17*, 880-892.

Choi, C.K., Vicente-Manzanares, M., Zareno, J., Whitmore, L.A., Mogilner, A., and Horwitz, A.R. (2008). Actin and alpha-actinin orchestrate the assembly and maturation of nascent adhesions in a myosin II motor-independent manner. Nat Cell Biol.

Chrzanowska-Wodnicka, M., and Burridge, K. (1996). Rho-stimulated contractility drives the formation of stress fibers and focal adhesions. J Cell Biol *133*, 1403-1415.

Deakin, N.O., and Turner, C.E. (2008). Paxillin comes of age. J Cell Sci *121*, 2435-2444.

del Rio, A., Perez-Jimenez, R., Liu, R., Roca-Cusachs, P., Fernandez, J.M., and Sheetz, M.P. (2009). Stretching single talin rod molecules activates vinculin binding. Science *323*, 638-641.

Digman, M.A., Wiseman, P.W., Choi, C., Horwitz, A.R., and Gratton, E. (2009). Stoichiometry of molecular complexes at adhesions in living cells. Proc Natl Acad Sci U S A *106*, 2170-2175.
Discher, D.E., Janmey, P., and Wang, Y.L. (2005). Tissue cells feel and respond to the stiffness of their substrate. Science *310*, 1139-1143.
Elosegui-Artola, A., Oria, R., Chen, Y., Kosmalska, A., Perez-Gonzalez, C., Castro, N., Zhu, C., Trepat, X., and Roca-Cusachs, P. (2016). Mechanical regulation of a molecular clutch defines force transmission and transduction in response to matrix rigidity. Nat Cell Biol *18*, 540-548.
Gardel, M.L., Schneider, I.C., Aratyn-Schaus, Y., and Waterman, C.M. (2010). Mechanical integration of actin and adhesion dynamics in cell migration. Annu Rev Cell Dev Biol *26*, 315-333.
Geiger, B., Spatz, J.P., and Bershadsky, A.D. (2009). Environmental sensing through focal adhesions. Nat Rev Mol Cell Biol *10*, 21-33.
Gingras, A.R., Bate, N., Goult, B.T., Patel, B., Kopp, P.M., Emsley, J., Barsukov, I.L., Roberts, G.C., and Critchley, D.R. (2010). Central region of talin has a unique fold that binds vinculin and actin. J Biol Chem *285*, 29577-29587.
Golji, J., and Mofrad, M.R. (2013). The interaction of vinculin with actin. PLoS Comput Biol *9*, e1002995.
Goult, B.T., Yan, J., and Schwartz, M.A. (2018). Talin as a mechanosensitive signaling hub. J Cell Biol *217*, 3776-3784.
Goult, B.T., Zacharchenko, T., Bate, N., Tsang, R., Hey, F., Gingras, A.R., Elliott, P.R., Roberts, G.C., Ballestrem, C., Critchley, D.R.*, et al.* (2013). RIAM and vinculin binding to talin are mutually exclusive and regulate adhesion assembly and turnover. J Biol Chem *288*, 8238-8249.
Gutierrez, E., Tkachenko, E., Besser, A., Sundd, P., Ley, K., Danuser, G., Ginsberg, M.H., and Groisman, A. (2011). High refractive index silicone gels for simultaneous total internal reflection fluorescence and traction force microscopy of adherent cells. PLoS One *6*, e23807.
Hakonardottir, G.K., Lopez-Ceballos, P., Herrera-Reyes, A.D., Das, R., Coombs, D., and Tanentzapf, G. (2015). In vivo quantitative analysis of Talin turnover in response to force. Mol Biol Cell *26*, 4149-4162.
Han, S.J., Bielawski, K.S., Ting, L.H., Rodriguez, M.L., and Sniadecki, N.J. (2012). Decoupling substrate stiffness, spread area, and micropost density: a close spatial relationship between traction forces and focal adhesions. Biophys J *103*, 640-648.
Han, S.J., Oak, Y., Groisman, A., and Danuser, G. (2015). Traction microscopy to identify force modulation in subresolution adhesions. Nat Methods *12*, 653-656.
Hu, Y.L., Lu, S., Szeto, K.W., Sun, J., Wang, Y., Lasheras, J.C., and Chien, S. (2014). FAK and paxillin dynamics at focal adhesions in the protrusions of migrating cells. Scientific reports *4*, 6024.
Huang, D.L., Bax, N.A., Buckley, C.D., Weis, W.I., and Dunn, A.R. (2017). Vinculin forms a directionally asymmetric catch bond with F-actin. Science *357*, 703-706.
Humphrey, J.D., Dufresne, E.R., and Schwartz, M.A. (2014). Mechanotransduction and extracellular matrix homeostasis. Nat Rev Mol Cell Biol *15*, 802-812.
Humphries, J.D., Wang, P., Streuli, C., Geiger, B., Humphries, M.J., and Ballestrem, C. (2007). Vinculin controls focal adhesion formation by direct interactions with talin and actin. J Cell Biol *179*, 1043-1057.
Kanchanawong, P., Shtengel, G., Pasapera, A.M., Ramko, E.B., Davidson, M.W., Hess, H.F., and Waterman, C.M. (2010). Nanoscale architecture of integrin-based cell adhesions. Nature *468*, 580-584.
Krawczyk, B. (2016). Learning from imbalanced data: open challenges and future directions. Progress in Artificial Intelligence *5*, 221-232.
Kumar, A., Ouyang, M., Van den Dries, K., McGhee, E.J., Tanaka, K., Anderson, M.D., Groisman, A., Goult, B.T., Anderson, K.I., and Schwartz, M.A. (2016). Talin tension sensor

reveals novel features of focal adhesion force transmission and mechanosensitivity. J Cell Biol *213*, 371-383.
Kuo, J.C., Han, X., Hsiao, C.T., Yates, J.R., 3rd, and Waterman, C.M. (2011). Analysis of the myosin-II-responsive focal adhesion proteome reveals a role for beta-Pix in negative regulation of focal adhesion maturation. Nat Cell Biol *13*, 383-393.
L. Allwein, E., E. Schapire, R., and Singer, Y. (2001). Reducing Multiclass to Binary: A Unifying Approach for Margin Classifiers, Vol 1.
Laukaitis, C.M., Webb, D.J., Donais, K., and Horwitz, A.F. (2001). Differential dynamics of alpha 5 integrin, paxillin, and alpha-actinin during formation and disassembly of adhesions in migrating cells. J Cell Biol *153*, 1427-1440.
Lawson, C., Lim, S.T., Uryu, S., Chen, X.L., Calderwood, D.A., and Schlaepfer, D.D. (2012). FAK promotes recruitment of talin to nascent adhesions to control cell motility. J Cell Biol *196*, 223-232.
Lee, H.S., Lim, C.J., Puzon-McLaughlin, W., Shattil, S.J., and Ginsberg, M.H. (2009). RIAM activates integrins by linking talin to ras GTPase membrane-targeting sequences. J Biol Chem *284*, 5119-5127.
Mitra, S.K., and Schlaepfer, D.D. (2006). Integrin-regulated FAK-Src signaling in normal and cancer cells. Curr Opin Cell Biol *18*, 516-523.
Morimatsu, M., Mekhdjian, A.H., Chang, A.C., Tan, S.J., and Dunn, A.R. (2015). Visualizing the interior architecture of focal adhesions with high-resolution traction maps. Nano Lett *15*, 2220-2228.
Moser, M., Legate, K.R., Zent, R., and Fassler, R. (2009). The tail of integrins, talin, and kindlins. Science *324*, 895-899.
Parsons, J.T. (2003). Focal adhesion kinase: the first ten years. J Cell Sci *116*, 1409-1416.
Parsons, J.T., Horwitz, A.R., and Schwartz, M.A. (2010). Cell adhesion: integrating cytoskeletal dynamics and cellular tension. Nat Rev Mol Cell Biol *11*, 633-643.
Pasapera, A.M., Schneider, I.C., Rericha, E., Schlaepfer, D.D., and Waterman, C.M. (2010). Myosin II activity regulates vinculin recruitment to focal adhesions through FAK-mediated paxillin phosphorylation. J Cell Biol *188*, 877-890.
Plotnikov, S.V., Pasapera, A.M., Sabass, B., and Waterman, C.M. (2012). Force fluctuations within focal adhesions mediate ECM-rigidity sensing to guide directed cell migration. Cell *151*, 1513-1527.
Riveline, D., Zamir, E., Balaban, N.Q., Schwarz, U.S., Ishizaki, T., Narumiya, S., Kam, Z., Geiger, B., and Bershadsky, A.D. (2001). Focal contacts as mechanosensors: externally applied local mechanical force induces growth of focal contacts by an mDia1-dependent and ROCK-independent mechanism. J Cell Biol *153*, 1175-1186.
Saltel, F., Mortier, E., Hytonen, V.P., Jacquier, M.C., Zimmermann, P., Vogel, V., Liu, W., and Wehrle-Haller, B. (2009). New PI(4,5)P2- and membrane proximal integrin-binding motifs in the talin head control beta3-integrin clustering. J Cell Biol *187*, 715-731.
Schiller, H.B., Friedel, C.C., Boulegue, C., and Fassler, R. (2011). Quantitative proteomics of the integrin adhesome show a myosin II-dependent recruitment of LIM domain proteins. EMBO Rep *12*, 259-266.
Schiller, H.B., Hermann, M.R., Polleux, J., Vignaud, T., Zanivan, S., Friedel, C.C., Sun, Z., Raducanu, A., Gottschalk, K.E., Thery, M.*, et al.* (2013). beta1- and alphav-class integrins cooperate to regulate myosin II during rigidity sensing of fibronectin-based microenvironments. Nat Cell Biol *15*, 625-636.
Schlaepfer, D.D., and Mitra, S.K. (2004). Multiple connections link FAK to cell motility and invasion. Curr Opin Genet Dev *14*, 92-101.
Shattil, S.J., Kim, C., and Ginsberg, M.H. (2010). The final steps of integrin activation: the end game. Nat Rev Mol Cell Biol *11*, 288-300.

Stricker, J., Aratyn-Schaus, Y., Oakes, P.W., and Gardel, M.L. (2011). Spatiotemporal constraints on the force-dependent growth of focal adhesions. Biophys J *100*, 2883-2893.
Sun, Z., Guo, S.S., and Fassler, R. (2016). Integrin-mediated mechanotransduction. J Cell Biol *215*, 445-456.
Tadokoro, S., Shattil, S.J., Eto, K., Tai, V., Liddington, R.C., de Pereda, J.M., Ginsberg, M.H., and Calderwood, D.A. (2003). Talin binding to integrin beta tails: a final common step in integrin activation. Science *302*, 103-106.
Thievessen, I., Thompson, P.M., Berlemont, S., Plevock, K.M., Plotnikov, S.V., Zemljic-Harpf, A., Ross, R.S., Davidson, M.W., Danuser, G., Campbell, S.L.*, et al.* (2013). Vinculin-actin interaction couples actin retrograde flow to focal adhesions, but is dispensable for focal adhesion growth. J Cell Biol *202*, 163-177.
Thomas, W. (2008). Catch bonds in adhesion. Annu Rev Biomed Eng *10*, 39-57.
Thomas, W.E., Vogel, V., and Sokurenko, E. (2008). Biophysics of catch bonds. Annu Rev Biophys *37*, 399-416.
Tschammer, N., Galinec, S., Weigert, S., Muller, Y., You, C., Piehler, J., and Breitsprecher, D. (2016). One-step, purification-free and site-specific labeling of polyhistidine-tagged proteins for MST. Protein Labeling.
Turner, C.E., Glenney, J.R., Jr., and Burridge, K. (1990). Paxillin: a new vinculin-binding protein present in focal adhesions. J Cell Biol *111*, 1059-1068.
Vogel, V., and Sheetz, M. (2006). Local force and geometry sensing regulate cell functions. Nat Rev Mol Cell Biol *7*, 265-275.
Webb, D.J., Donais, K., Whitmore, L.A., Thomas, S.M., Turner, C.E., Parsons, J.T., and Horwitz, A.F. (2004). FAK-Src signalling through paxillin, ERK and MLCK regulates adhesion disassembly. Nat Cell Biol *6*, 154-161.
Whitewood, A.J., Singh, A.K., Brown, D.G., and Goult, B.T. (2018). Chlamydial virulence factor TarP mimics talin to disrupt the talin-vinculin complex. FEBS letters *592*, 1751-1760.
Wiseman, P.W., Brown, C.M., Webb, D.J., Hebert, B., Johnson, N.L., Squier, J.A., Ellisman, M.H., and Horwitz, A.F. (2004). Spatial mapping of integrin interactions and dynamics during cell migration by image correlation microscopy. J Cell Sci *117*, 5521-5534.
Yan, J., Yao, M., Goult, B.T., and Sheetz, M.P. (2015). Talin Dependent Mechanosensitivity of Cell Focal Adhesions. Cell Mol Bioeng *8*, 151-159.
Yao, M., Goult, B.T., Chen, H., Cong, P., Sheetz, M.P., and Yan, J. (2014). Mechanical activation of vinculin binding to talin locks talin in an unfolded conformation. Scientific reports *4*, 4610.
Yao, M., Goult, B.T., Klapholz, B., Hu, X., Toseland, C.P., Guo, Y., Cong, P., Sheetz, M.P., and Yan, J. (2016). The mechanical response of talin. Nature communications *7*, 11966.
Zacharchenko, T., Qian, X., Goult, B.T., Jethwa, D., Almeida, T.B., Ballestrem, C., Critchley, D.R., Lowy, D.R., and Barsukov, I.L. (2016). LD Motif Recognition by Talin: Structure of the Talin-DLC1 Complex. Structure *24*, 1130-1141.
Zaidel-Bar, R., Cohen, M., Addadi, L., and Geiger, B. (2004). Hierarchical assembly of cell-matrix adhesion complexes. Biochem Soc Trans *32*, 416-420.
Zhu, J., Luo, B.H., Xiao, T., Zhang, C., Nishida, N., and Springer, T.A. (2008). Structure of a complete integrin ectodomain in a physiologic resting state and activation and deactivation by applied forces. Mol Cell *32*, 849-861.